atmosphere

MDPI

Article

The Role of the Indian Ocean Basin-Wide and El Niño–Southern Oscillation Modes in Interannual Rainfall Variability over South America during Austral Summer

Mary T. Kayano [1,*], Rita V. Andreoli [2], Wilmar L. Cerón [3] and Rodrigo A. F. Souza [2]

[1] Coordenação Geral de Ciências da Terra, Instituto Nacional de Pesquisas Espaciais, Avenida dos Astronautas, 1758, São José dos Campos 12227-010, SP, Brazil
[2] Escola Superior de Tecnologia, Universidade do Estado do Amazonas, Av. Darcy Vargas, 1200, Parque 10 de Novembro, Manaus 69065-020, AM, Brazil; rasouza@uea.edu.br (R.V.A.); rafsouza@uea.edu.br (R.A.F.S.)
[3] Department of Geography, Faculty of Humanities, Universidad del Valle, Calle 13 # 100-00, Cali P.O. Box 25360, Colombia; wilmar.ceron@correounivalle.edu.co
* Correspondence: mary.kayano@inpe.br; Tel.: +55-12-32086658

Abstract: This paper examines the relative role of the Indian Ocean basin-wide (IOBW) mode and El Niño–Southern Oscillation (ENSO) in the atmospheric circulation and rainfall interannual variations over South America (SA) during southern summer of the 1951-2016 period. The effects of the warm IOBW and El Niño (EN) events, and of the cold IOBW and La Niña (LN) events are examined using partial correlations. The ENSO and IOBW modes, through the associated large-scale and regional anomalous circulation patterns, induce contrasting effects on the rainfall in northeastern SA. The EN without the warm IOBW effect induces anomalously dry conditions over eastern Amazon and part of northeastern Brazil (NEB) through anomalous sinking motions of the EN-related anomalous Walker and Hadley cells and strong moisture divergence associated with a vigorous anticyclone over tropical South Atlantic (TSA) and SA. The warm IOBW without the EN effect induces anomalously wet conditions in NEB, which is marginally related to the anomalous Walker and Hadley cells but is modulated by an anticyclone over SA between the equator and 20° S, and a cyclone in the southwestern Atlantic between 20° S and 40° S. The results here might be relevant for climate monitoring and modeling studies.

Keywords: climate variability; South America; rainfall; teleconnections; tropical Indian ocean; Rossby wave train; ENSO

Citation: Kayano, M.T.; Andreoli, R.V.; Cerón, W.L.; Souza, R.A.F. The Role of the Indian Ocean Basin-Wide and El Niño–Southern Oscillation Modes in Interannual Rainfall Variability over South America during Austral Summer. *Atmosphere* **2021**, *12*, 1094. https://doi.org/10.3390/atmos12091094

Academic Editor: Indrani Roy

Received: 23 July 2021
Accepted: 22 August 2021
Published: 25 August 2021

1. Introduction

As a natural climate forcing, the El Niño–Southern Oscillation (ENSO) is the most prominent phenomenon that modulates interannual climate variability on a global scale. Particularly in South America (SA), ENSO drives rainfall anomalies in the tropical sector through changes in the Walker cell and local Hadley cell [1,2] and in the subtropical and extratropical sectors through ENSO-induced Rossby wave train teleconnection patterns [3,4]. The El Niño (EN) related eastward-shifted Walker cell reduces rising motions over equatorial SA, creating favorable conditions for droughts [5–7]. Meanwhile, a stronger than normal subtropical jet stream over southeastern SA (SESA) [8], acting together with an upper-tropospheric blocking in the region [6], is responsible for abnormal wetness in this region during the southern spring and summer of the EN years. These atmospheric patterns are also accompanied by an intensified South American Low-Level Jet (SALLJ) along the eastern side of the Andes Mountains, which transports moisture from the Amazon into subtropical SA [1]. The rainfall in SA is also modulated by the EN-induced Rossby wave train pattern in the Southern Hemisphere extending over the southeastern Pacific and SA, which is called Pacific–South American (PSA) teleconnection pattern [3]. During early summer, the low-level anomalous anticyclone in central Brazil, tropics, and subtropics

associated with the PSA, Walker, and Hadley cells induces negative rainfall anomalies in northern and central Brazil and positive rainfall anomalies in southern Brazil [9]. Additionally, results of more detailed studies of the ENSO impacts on the South American rainfall documented regional effects of surface–atmosphere interactions in central-eastern SA, with reversed signs of the rainfall anomalies from spring to summer [10]. In general, the La Niña (LN) related atmospheric circulation and rainfall anomalies over SA show opposite sign patterns as those documented for the EN [11]. For an extensive review of the ENSO impacts on the South American rainfall, the reader is referred to Cai et al. [12].

Besides, ENSO might also modulate the sea surface temperature (SST) anomalies in other tropical oceans through the atmospheric bridge and the oceanic processes [13]. Indeed, EN causes wind variations in the western Pacific and neighboring areas, with anomalous anticyclonic wind stress on the eastern Indian Ocean, which intensifies the net heat flux into the ocean, thus warming this side of the basin, and induces oceanic downwelling Rossby waves, which propagate westward and warm the Indian basin 3–4 months later [14]. The uniform warming or cooling of the tropical Indian Ocean is the dominant interannual variability mode in this basin [14] and plays an important role in the regional and remote climate variations through changes in the tropical and extratropical circulation anomaly patterns [15–17]. This mode, called the Indian Ocean basin-wide (IOBW), shows its largest variability during southern summer and autumn [18,19]. It is mostly ENSO-induced [18,19], with EN inducing a warm IOBW event and LN, a cold IOBW event [20]. Taschetto and Ambrizzi [17] provided modeling and diagnostic evidence on the warm IOBW events' contribution to strengthening the EN-related atmospheric circulation and rainfall anomalies over SA through the Walker cell and Rossby wave train teleconnection pattern during southern autumn. They also argued that the warm IOBW event is responsible for the persistent dryness over northeastern Brazil (NEB).

Another variability mode in the tropical Indian Ocean, called the Indian Ocean dipole, features an east–west dipolar structure of the SST anomalies independent of the ENSO [21,22]. It presents its largest variability during southern winter and spring and its maximum intensity during spring [21]. This mode modulates rainfall in many regions such as South Asia [23], eastern Africa [24], southeastern Africa [25], and eastern SA and SESA [26,27]. The positive dipole excites a Rossby wave train pattern that connects the tropical Indian Ocean and SA across the southern mid-latitude waveguide. It affects the South American climate [26], through a low-level anticyclone in the southwestern subtropical Atlantic that channels moisture from central Brazil to the La Plata Basin, causing rainfall deficits over the South Atlantic convergence zone area and excessive rainfall over the La Plata Basin during southern spring [27].

From the abovementioned, the Indian Ocean SST variability modes affect rainfall of equatorial and subtropical SA, where many socio-economic activities with high demand on water availability take place. Notwithstanding, only a few studies can be found in the literature on the teleconnections between the Indian Ocean variability and the South American climate. Drumond and Ambrizzi [28] documented a relationship between the subtropical Indian Ocean warming and rainfall increase in subtropical SA during southern summer. Additionally, relationships between the tropical Pacific and Indian Oceans and the rainfall in the western side of southern SA during austral winter were registered [29,30]. On the other hand, Berman et al. [31] found low-frequency linkages between the SST in the Indian Ocean and rainfall in southern SA, in the decadal time scale for the eastern and central subtropical Indian Ocean, and interdecadal time scale for the eastern tropical and western subtropical Indian Ocean.

The SST variations in the Indian Ocean at decadal to interdecadal time scales were confirmed later [32,33]. In addition to this, the Indian Ocean has shown a warming trend since the 1950s [34–37], which has been attributed to anthropogenic forcing [32,33,36]. Thus, studies focusing on the relations of the Indian Ocean and the South American climate variations should consider the temporal variability and trend of the SST in the Indian Ocean. Additionally, ENSO has a dominant effect on South American rainfall variability

in relation to other variability modes. In this vein, to isolate the effect of individual ocean basins, Taschetto and Ambrizzi [17] used numerical experiments in addition to statistical methods.

The relationships of the IOBW mode and the South American rainfall variability deserve further analysis. A question that was not answered yet is the relative role of the IOBW and ENSO in South American rainfall during its rainy season. Since the rainy season in large portions of SA peaks during southern summer [38], and the largest variability of the IOBW mode [19] and ENSO mature stage [39] occur in this season, the present analysis focused on southern summer. As the IOBW and ENSO modes are closely connected [18,19], partial correlation analyses were used to examine the relative role of the IOBW and ENSO modes in the rainfall and atmospheric circulation variations over SA.

2. Data and Methods

The SST data were extracted from the National Oceanic and Atmospheric Administration extended reconstructed SST version V5 dataset [40,41]. The SST data are in a 2° horizontal resolution grid. The rainfall data were obtained from the Global Precipitation Climatology Centre Full Data Reanalysis V.8 version dataset [42,43]. In this reanalysis, the rain gauge station coverage varies during the period with available data, with a dense network after 1950 [42]. Considering this data limitation, the present analysis is for the 1951–2016 period, so all data were obtained for this period. The rainfall data on a 1° horizontal resolution grid were used. The atmospheric variables were obtained from the National Centers for Environmental Prediction/National Center for Atmospheric Research Reanalysis-I Project dataset [44,45]. These data are in a 2.5° horizontal resolution grid and at 11 standard surface pressure levels (1000, 925, 850, 700, 600, 500, 400, 300, 250, 200, and 150 hPa). The zonal and meridional winds plus specific humidity at the first eight lower levels and vertical velocity in pressure coordinates (VVEL) at the first 10 lower levels were used. In the results, the 850 hPa zonal and meridional wind vector is referred to as WND850. The streamfunction (PSI) data derived from the horizontal winds in a Gaussian grid of 192 by 94 points at sigma levels 0.8458 and 0.2101 were also used. These sigma levels correspond approximately to 850 and 200 hPa, respectively, so that the PSI at these levels were referred to as PSI850 and PSI200. The asymmetric PSI data were used. The vertically integrated moisture flux components and their divergence were calculated using the equations after Peixoto and Oort [46]. In the results, this vector is referred to as VIMF. The vertical integration to calculate VIMF was done from surface to 300 hPa. The vertical velocities averaged in the 5° N–5° S sector represent the Walker cell, and the vertical velocities averaged in the 60° W–35° W sector, the regional Hadley cell. Before anomaly calculations, the linear trends over the 1951–2016 period were removed from the monthly data in each grid point.

Since analyses were completed for December–January–February (DJF), first, DJF average values for all variables were obtained. Then, seasonal standardized anomaly time series were calculated by considering the means and standard deviations of the 1951–2016 period. Finally, the interannual time scale in the anomaly time series was isolated by applying a Morlet wavelet bandpass filter (2–7 year). The Morlet wavelet is a complex exponential modulated by a Gaussian, $e^{i\omega_o\eta}e^{-\eta^2/2}$, with $\eta = t/s$, where t is the time, s is the wavelet scale, and ω_o is a non-dimensional frequency [47]. The filtered time series is calculated using equation 29 in Torrence and Compo [47]. Calculations were made separately for each variable and grid point.

Taschetto and Ambrizzi [17] used the Niño-3 SST index and defined the IOBW index as the principal component (PC) time series of the first empirical orthogonal function (EOF) mode of the monthly SST anomalies in the tropical Indian Ocean. For better representation of the seasonality of the IOBW and ENSO modes, here, the EOF analysis of the filtered summer SST anomalies over the 1951–2016 period was applied separately in each oceanic sector. The tropical Indian Ocean is the area limited at 26° N, 26° S, 30° E, and 120° E, and the tropical Pacific Ocean, at 30° N, 30° S, 110° E, and 70° W. It will be clear in the

results that the main mode in the tropical Indian Ocean represents the IOBW mode, and the main mode in the tropical Pacific, the ENSO mode. Then, the PC time series of the main mode in each oceanic sector was used as an index. In the EOF analysis, the covariance matrix and North et al. [48] criterium for examining the separation of the eigenvalues were used. The eigenvectors were displayed as correlation patterns. The statistical significance of these correlations was assessed with Student's *t*-test for 66 degrees of freedom [49]. This test gives the threshold of 0.25, for the significant correlations at a 95% confidence level. Since the warm IOBW relates to the EN, and the cold IOBW to the LN, whenever necessary, the PC time series was multiplied by −1 so that the warm events in the two tropical oceanic sectors were represented by positive values of the corresponding PC time series. For conciseness, the oceanic indices are referred to as IOBW for the Indian Ocean PC and TPO for the tropical Pacific Ocean PC.

Finally, the partial correlation coefficients (PCC) between the oceanic indices and the variable anomaly time series were calculated for the 1951–2016 period. The statistical significance of the correlations was assessed using Student's *t*-test at a 95% confidence level. Henceforth, the word 'interannual' regarding the interannual variable anomalies is omitted; the PCC of the oceanic index-1 and a given variable, while excluding the influence of the oceanic index-2, is referred to as PCC of oceanic index-1 and the given variable. Correlations might be interpreted as variable anomalies if the phase of the index, for which the correlations are calculated, is specified. This approach is adopted when interpreting correlation maps.

3. Results

3.1. EOF Modes of the SST Anomalies in the Tropical Indian and Pacific Oceans

The corresponding loading pattern and PC time series of the first EOF mode of the SST anomalies in the tropical Pacific during summer are shown in Figure 1. This mode explains 41.1% of the interannual summer SST variances, and according to North et al.'s [48] criterion is well separated from the other modes. This mode discloses the loading pattern similar to the SST anomaly pattern previously registered during the EN mature stage [39,50]. For positive PC values, this mode shows the largest positive SST anomalies in the central-eastern tropical Pacific area limited at the 10°N–10°S band between the dateline longitude and 120°W (Figure 1). The PC time series of this mode shows ENSO related interannual fluctuations with the highest positive values during 1972–1973, 1982–1983, 1997–1998, and 2009–2010 EN summers, which were very strong events, and the highest negative values during the 1970–1971 and 1988–1989 LN summers. Additionally, secondary positive PC values occur during 1957–1958, 1965–1966, and 1987–1988 EN summers. The PC time series is used as the ENSO index and referred to as the TPO index.

The loading pattern and the PC time series of the first EOF mode of the SST anomalies in the tropical Indian Ocean during summer are illustrated in Figure 2. This mode explains 49.7% of the summer interannual SST variance, and according to North et al.'s [48] criterium, it is well separated from the other modes. It reproduces the SST anomaly features previously described for the warm IOBW mode [14]. Indeed, for the positive PC values, this mode discloses positive SST anomalies in the tropical Indian Ocean with the largest loading values in its eastern side between 10°N and the equator (Figure 2). The corresponding PC time series show interannual fluctuations with the higher positive values coinciding with EN occurrences and the higher negative values with LN occurrences. This result confirms the close relations between the IOBW and ENSO modes [18,19], with EN relating to a warm IOBW event, and LN, to a cold IOBW event [20]. These time series show larger magnitudes of positive than negative values, with the largest positive values during 1972–1973, 1997–1998, and 2009–2010 EN summers, and the largest negative values during the 1970–1971 and 2010–2011 LN summers. This result is consistent with the asymmetry of the ENSO, such that EN events are stronger than LN events [51]. It is also noticeable that the secondary largest positive values coincide with 1957–1958, 1963–1964, 1969–1970, 1982–1983 EN summers, with the latest summer marked by a strong EN event, and the

others by moderate or weak EN events. The PC time series of the first mode is used as the IOBW index, and hereafter referred to as the IOBW index. The correlation coefficient between the TPO and IOBW indices is 0.9 and confirms the close relations between the ENSO and IOBW modes.

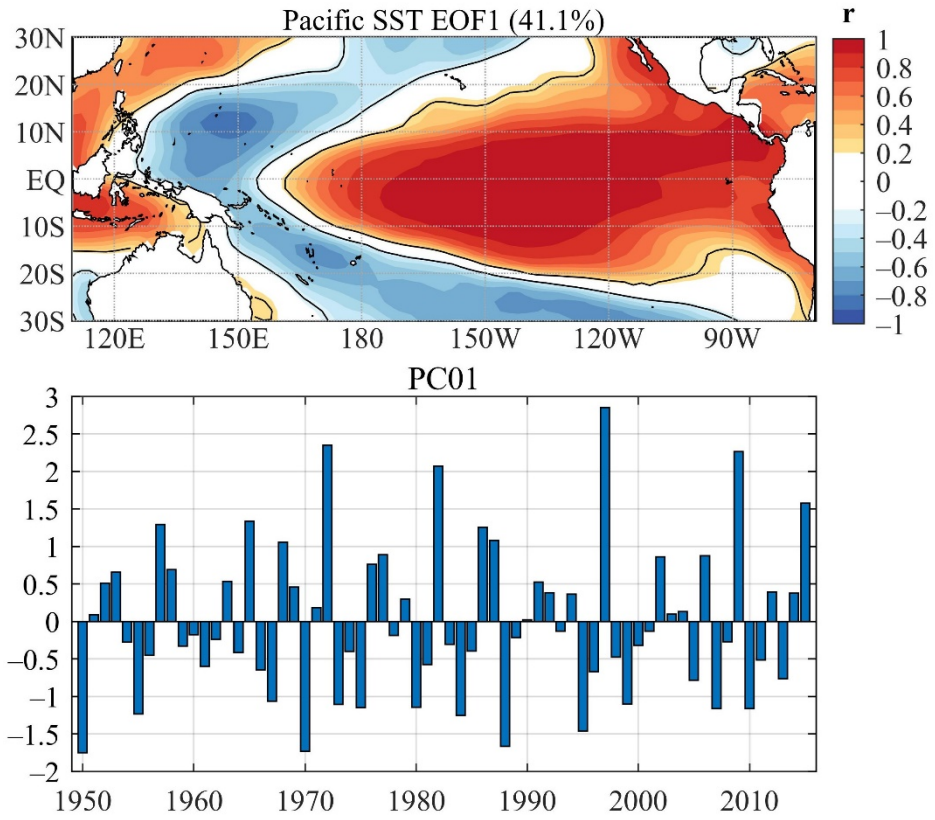

Figure 1. First EOF mode of the interannual SST anomalies in the tropical Pacific Ocean computed for the southern summers of the 1951–2016 period: spatial loading pattern and principal component (PC) time series. Continuous line encompasses the significant correlations at a 95% confidence level using Student's *t*-test.

In the next sections, the relationships between the oceanic indices and the variables are investigated using PCC analyses. The positive values of the TPO and IOBW indices correspond to the warm modes in the tropical Pacific and Indian Oceans, respectively. Therefore, for the positive (negative) TPO values, the PCC of the TPO and a given variable represent the relation of EN (LN) and a given variable without the warm (cold) IOBW event effect. Conversely, for the positive (negative) IOBW values, the PCC of the IOBW and a given variable represents the relation of the warm (cold) IOBW event and a given variable without the EN (LN) effect. Therefore, for a given phase of the TPO or IOBW indices, we may refer to anomalies of the variable instead of correlations.

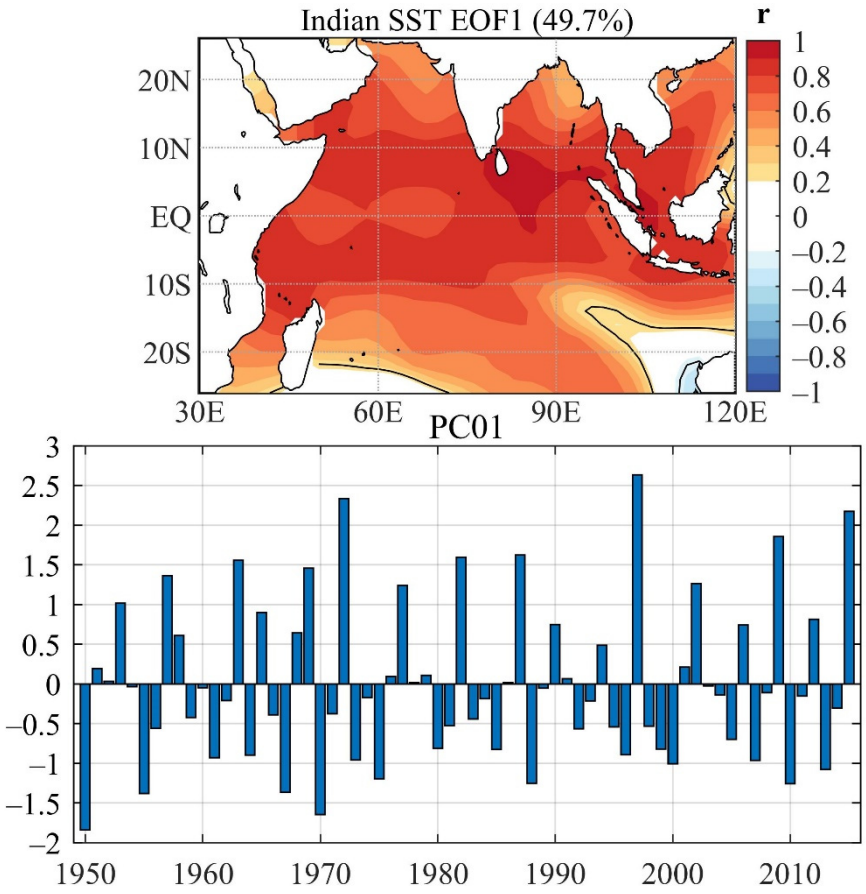

Figure 2. First EOF mode of the interannual SST anomalies in the tropical Indian Ocean computed for the southern summers of the 1951–2016 period: spatial loading pattern and principal component (PC) time series. Graphical display is the same as that in Figure 1.

3.2. SST Anomaly Patterns

The maps of the PCC of the TPO and SST and of the IOBW and SST are shown in Figure 3a,b, respectively. As expected, for the positive TPO, the PCCs of the TPO and SST (Figure 3a) reproduce the EN-related SST anomaly pattern in the tropical Pacific illustrated above (Figure 1) and no consistent signature of the warm IOBW mode (Figure 2). It is also interesting to note that the Indian Ocean Dipole (IOD), like the SST pattern, appears in the Indian Ocean when the IOBW effect is removed from the SST anomalies (Figure 3a). The IOD mode is the second mode of the SST variability in the Indian Ocean (figure not shown). Since this mode is not the focus of the present analysis, it was not analyzed. On the other hand, for the positive IOBW, the pattern of the PCC of the IOBW and SST (Figure 3b) resembles the warm IOBW mode pattern disclosed above in the tropical Indian Ocean (Figure 2) and does not show the EN pattern in the tropical Pacific (Figure 1). Therefore, the PCC analyses efficiently isolated from each other the TPO and IOBW effects on the global SST in the tropics. These results guarantee the robustness of the PCC analyses for other variables.

In the Atlantic, the PCC of the TPO and SST shows a correlation dipole with a negative northern node in the sector between 10° N and 10° S and the positive southern node between 10° S and 35° S (Figure 3a). The PCC of the IOBW and SST discloses approximately a reversed sign dipole, but with a more extensive positive northern node (between 10° N and 15° S) and a negative southern node in the 20° S-40° S band (Figure 3b). For a given phase of the TPO and IOBW indices, the corresponding SST anomaly dipole resembles the previously discussed anomalous SST South Atlantic dipole (SAD) mode [52,53] but is further north than the SAD mode. Similar to the SAD mode, the dipole identified here

might significantly affect the summer rainfall in the adjacent South American areas. This aspect is discussed below using other variables.

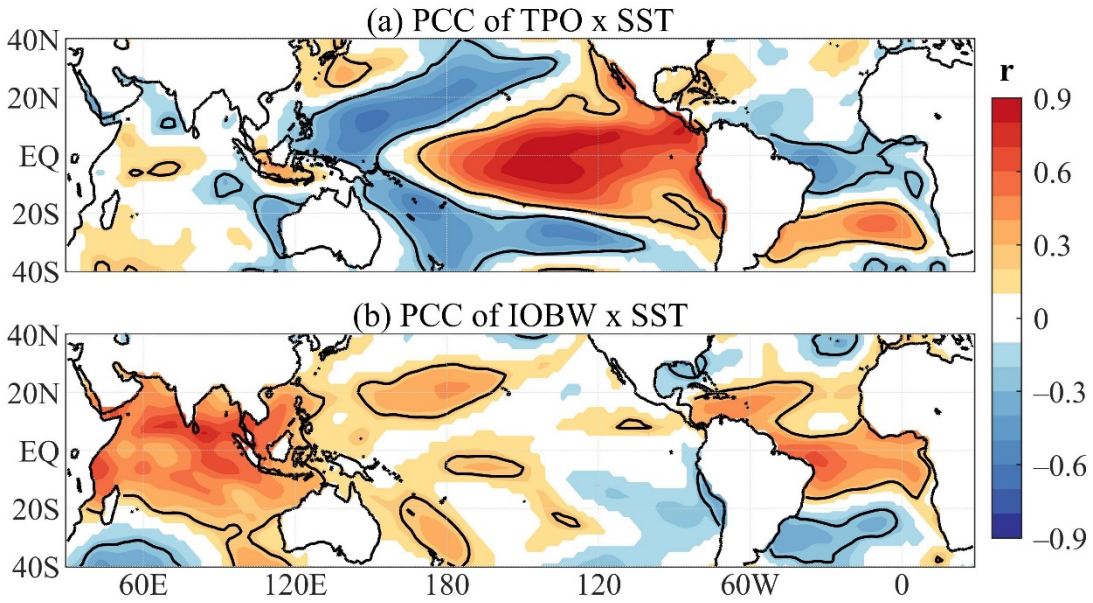

Figure 3. Partial correlations for SST during southern summer of the (**a**) TPO and SST; (**b**) IOBW and SST. Continuous line encompasses significant correlations at a 95% confidence level using the level using Student's *t*-test.

3.3. Atmospheric Circulation and Rainfall Anomaly Patterns

The longitude vertical cross-sections of the PCC of the oceanic indices and the VVEL anomalies averaged in the 5° N–5° S band show distinct features (Figure 4a,b). For the positive TPO, the PCCs of the TPO and VVEL describe an EN-related anomalous eastward-shifted Walker cell with rising motions in the central and eastern Pacific (160° E–80° W), flanked by sinking motions to the west (Indonesia–western Pacific) and to the east (80° W–15° E) (Figure 4a). Meanwhile, for positive IOBW, the PCCs of the IOBW and VVEL show a tripole with significant values in narrow longitudinal bands, with anomalous rising motions in the eastern Indian Ocean–Indonesia (100° E–110° E), central Pacific (170° W–160° W) and Atlantic (30° W–10° E), anomalous sinking motions in the 120° E–130° E band and mostly in the middle to upper levels of the 130° W–80° W band, and nearly neutral VVEL anomalies along the other longitudes (Figure 4b). One of the most relevant features for regional climate variability is the contrasting effects of the EN and warm IOBW events on the VVEL anomalies along the equatorial SA-Atlantic sector, with anomalous sinking motions for the TPO index and neutral to anomalous rising motions for the IOBW index (Figure 4a,b).

The latitude vertical cross-sections of the PCC of the oceanic indices and the VVEL anomalies averaged in the 60° W–35° W band disclose contrasting patterns (Figure 5a,b). For the positive TPO, the PCCs of the TPO and VVEL show an anomalous meridional circulation with sinking motions mostly in the 20° S–12° N band flanked by rising motions to the north of 25° N in all tropospheric levels and south of 25° S in the middle tropospheric levels (Figure 5a). On the other hand, for positive IOBW, the PCCs of the IOBW and VVEL depict anomalous rising motions approximately in the 22° S–7° S band with significant values limited to the 22° S–18° S band in the middle and upper tropospheric levels and the 26° S–22° S band in the low-levels, and anomalous sinking motions to the south of 25° S and north of 10° N, with significant values in vertically and meridionally more reduced areas (Figure 5b).

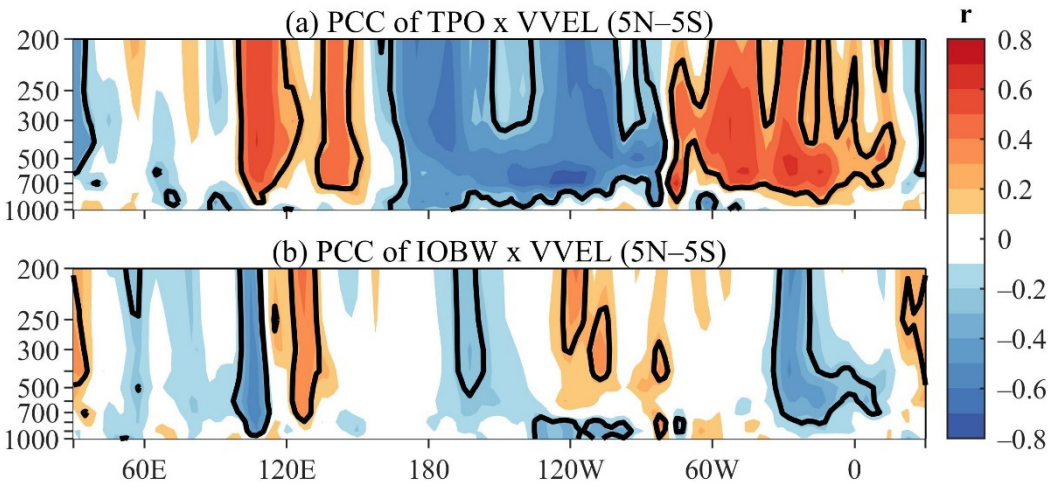

Figure 4. Longitude vertical cross-sections of the partial correlations for the vertical velocity in pressure coordinate averaged in the 5° N-5° S band (VVEL) during southern summer: (**a**) TPO and VVEL; (**b**) IOBW and VVEL. Continuous line encompasses significant correlations at a 95% confidence level using Student's *t*-test. The vertical pressure levels are in hPa.

The above results indicate that both the anomalous Walker and regional Hadley cells associated with the ENSO induce consistent VVEL anomalies over NEB and adjacent areas, with EN-related sinking motions, and LN-related rising motions. Meanwhile, for the IOBW an anomalous east–west equatorial cell more efficiently induces consistent VVEL anomalies over NEB with the warm IOBW mode related to rising motions and the cold IOBW mode to sinking motions. Consequently, there are expected differential IOBW and ENSO effects on the rainfall in SA, particularly in areas neighboring the equatorial Atlantic.

Figure 6a discloses the total correlation coefficients (TCC) map between the TPO index and the precipitation. It is worth recalling that the IOBW influence on the precipitation was not removed. The corresponding map of the TCC between the IOBW index and the precipitation (Figure not shown) shows very similar patterns as those presented in Figure 6a. For positive TPO, Figure 6a indicates rainfall deficits in most areas in northwestern and northern SA north of 5° and west of 50° W and in a meridionally extended area from central-eastern Peru to southwestern Bolivia, and excessive rainfall in SESA. This pattern closely resembles the EN-related rainfall anomaly pattern over SA in January shown in Grimm [9] (their Figure 6). The rainfall anomaly pattern inferred from Figure 6a was previously attributed to the EN-induced atmospheric circulation anomalies with the anomalous sinking motions associated with an eastward-displaced Walker cell justifying the rainfall deficits in equatorial SA [5–7], and an intensified SALLJ, through the associated regional moisture transport, the excessive rainfall in SESA [1,9]. Therefore, the TCC map of the TPO and rainfall (Figure 6a) describes the combined IOBW and ENSO effects on the South American rainfall, which have been pointed out as closely linked to the ENSO in earlier studies. Nevertheless, the IOBW and ENSO modes, both in warm or cold phases, acting independently, have distinct effects on the South American rainfall (Figure 6b,c).

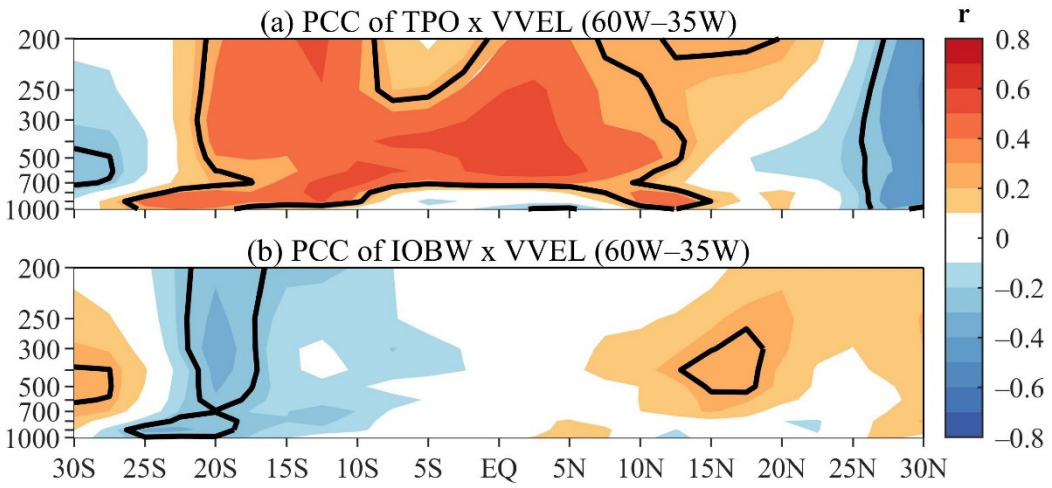

Figure 5. Latitude vertical cross-sections of the partial correlations for the vertical velocity in pressure coordinate averaged in the 60° W-35° W band (VVEL) during southern summer: (**a**) TPO and VVEL; (**b**) IOBW and VVEL. Graphical display is the same as that in Figure 4.

For the positive TPO, the map of the PCC of the TPO and rainfall discloses deficits in a large area extending from the eastern Amazon into most of NEB, excessive rainfall in part of SESA (Uruguay, southern Brazil, and northeastern Argentina), in addition to small areas with alternating anomalously dry and wet conditions in Colombia (Figure 6b). The rainfall deficits in the eastern Amazon and most of NEB are consistent with the anomalous sinking motions associated with the anomalous Walker and Hadley cells (Figures 4a and 5a). Consistent with this anomalous rainfall pattern and for positive TPO, the map of the PCC of the TPO and VIMF features strong moisture divergence over northern SA and the adjacent tropical North Atlantic (TNA), in areas from Colombia to northern Bolivia, in equatorial Atlantic and along eastern SA from the equator to approximately 20° S, and moisture convergence over eastern and southern Brazil, Uruguay and the adjacent oceanic areas, which are accompanied by a vigorous anomalous anticyclone over TSA and SA east of 60° W (Figure 7a). The flow associated with this anticyclone in the eastern Amazon splits into two branches, one blows westward into southern Amazon and the other along the vortex western edge follows southward in central-western Brazil and then southeastward into eastern and southern Brazil and Uruguay (Figure 7a). This second branch likely intensifies the SALLJ, which transports moisture from the Amazon southeastward into SESA, where convergent moisture flux and excessive rainfall occur (Figures 6b and 7a). This result is consistent with the previous finding regarding the EN effect on South American rainfall [1,2].

The map of the PCC of the IOBW and rainfall, for positive IOBW, presents a prominent area with positive rainfall anomalies throughout NEB and extreme eastern Amazon, and negative anomalies in small regions of Guiana, French Guiana, central-eastern Colombia, southern Peru, northern Chile and southeastern Brazil (Figure 6c). The excessive rainfall over NEB and extreme eastern Amazon seems to be marginally modulated by the anomalous Walker and Hadley cells, whose associated ascending branches are centered, respectively, further east and south of the excessive rainfall area (Figures 4b and 5b). In this case, moisture convergence is noted over the equatorial Atlantic and along eastern SA between the equator and 20° S, and moisture divergence over coastal areas of southeastern Brazil and the adjacent Atlantic, which are associated with an anticyclone over SA between the equator and 20° S, and a cyclone in the southwestern Atlantic between 20° S and 40° S, implying in the absence of the SALLJ (Figure 7b). These anomalous circulation patterns and the associated moisture transport explain the dryness over part of southeastern Brazil and the wetness over eastern NEB.

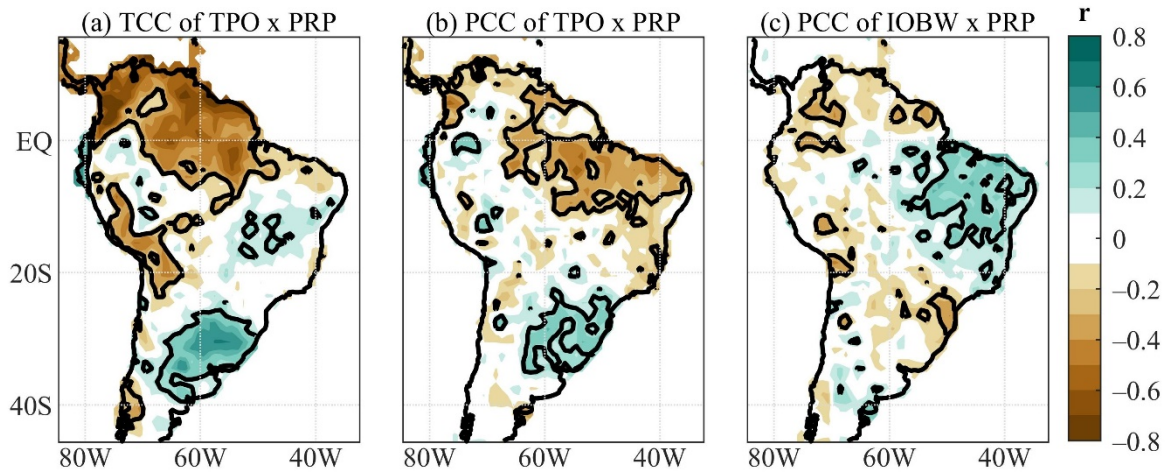

Figure 6. Correlations for the precipitation (PRP) during southern summer: (**a**) TCC of the TPO and PRP; (**b**) PCC of the TPO and PRP; (**c**) PCC of the IOBW and PRP. Continuous line encompasses significant correlations at a 95% confidence level using Student's *t*-test.

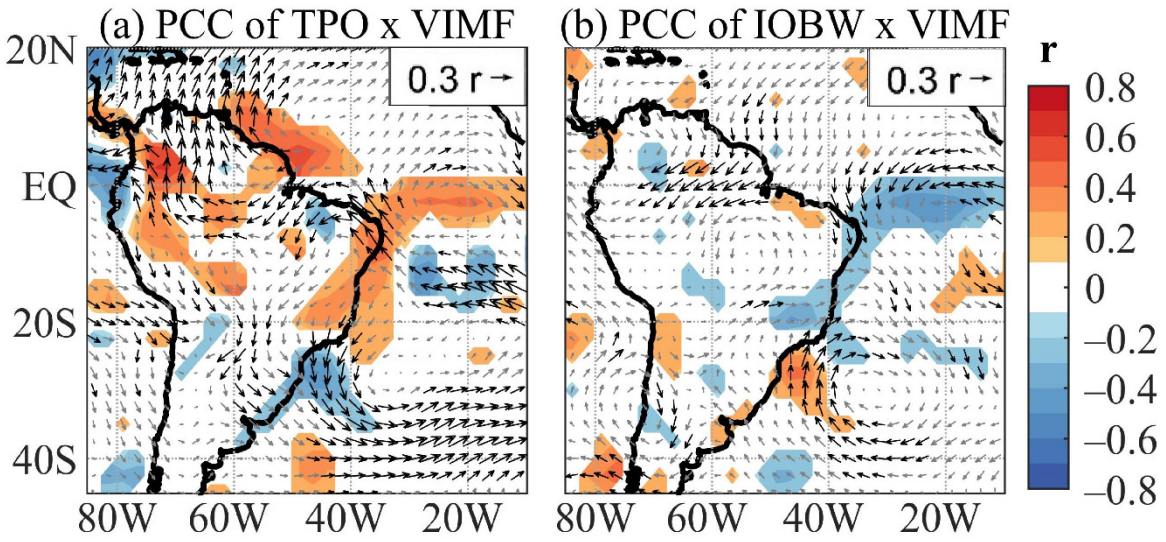

Figure 7. Partial correlations for the vertically integrated moisture flux (VIMF) components and their divergence (shades) during summer of the (**a**) TPO and VIMF; (**b**) IOBW and VIMF. Shades encompass significant correlations at a 95% confidence level using Student's *t*-test. Vectors indicate the correlations with the VIMF components. Arrow in the right-lower corner gives the vector base magnitude in correlation units. Bold arrows indicate vectors when at least one component has significant correlation at a 95% confidence level.

The results here indicate that the rainfall anomaly pattern inferred from Figure 6a reflects indeed the combined effects of the warm IOBW and EN events, which reinforce and/or better organize the rainfall anomalies in northwestern and northern SA, counteract in other areas such as in NEB and southeastern Brazil, but EN dominates the anomalous rainfall signal in SESA (Figure 6a–c).

Consistent with the abovementioned moisture transport, the map of the PCC of the TPO and WND850/SST (Figure 8a), for positive TPO, describes anomalous circulations in the tropical Atlantic, with anticyclones straddling the equator, one centered in the southeastern TNA and the other in the central TSA, this latter representing an intensified subtropical South Atlantic high (SASH) pressure system (Figure 8a). The associated SST correlations indicate a significant negative center in the western equatorial Atlantic and the positive one in the central TSA (Figure 8a). For positive IOBW, nearly antisymmetric patterns of circulation and SST anomalies are noted in the map of the PCC of the IOBW

and the WND850/SST (Figure 8a,b). The relationships between the SST and low-level wind anomalies are likely to involve wind–evaporation–SST (WES) effects and Ekman transport due to the wind variations. For positive TPO, the map of PCC of the TPO and WND850/SST features strengthened easterlies in the equatorial Atlantic associated with the anticyclones straddling the equator, which enhance the evaporation and induce the surface waters cooling in the western equatorial Atlantic; meanwhile, the intensified SASH pressure system in the TSA intensifies the Ekman pumping causing downwelling and warming up this area (Figure 8a).

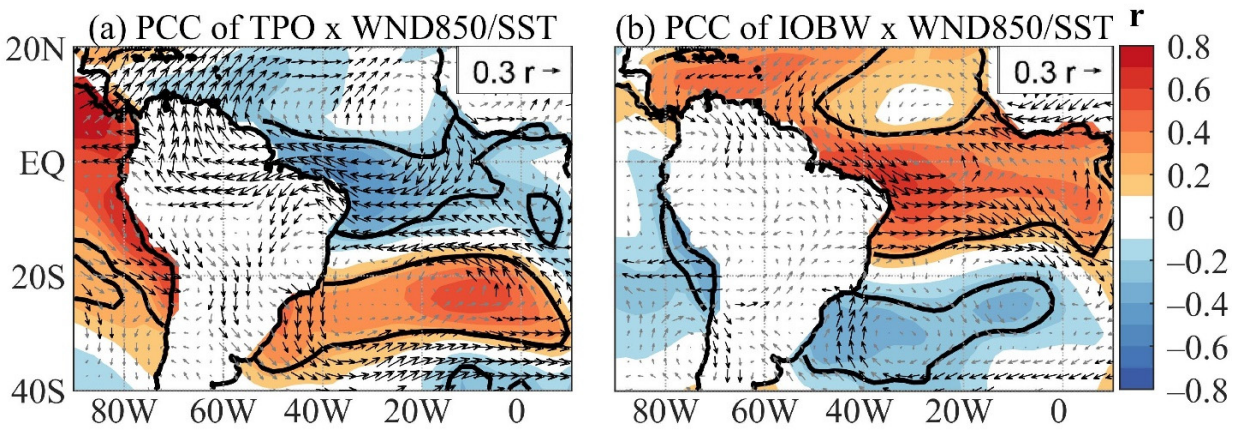

Figure 8. Partial correlations for the SST (shades) and 850 hPa horizontal winds (WND850) during summer of the (**a**) TPO and WND850/SST; (**b**) IOBW and WND850/SST. The continuous line encompasses significant correlations at a 95% confidence level using Student's *t*-test. The arrow in the right-lower corner gives the vector base magnitude in correlation units. Bold arrows indicate vectors when at least one component has a significant correlation at a 95% confidence level.

Conversely, for the positive IOBW, the map of PCC of the IOBW and WND850/SST shows weakened easterlies (or equivalently westerly anomalies) in the equatorial Atlantic, which reduce evaporation and induce warming there, and the weakened SASH pressure system intensifies the Ekman suction causing upwelling and cooling down this area (Figure 8b). In both cases, the SST anomaly pattern creates a meridional thermal contrast between the TSA and the equatorial Atlantic, which induces an anomalous thermally direct meridional cell discussed above (Figure 5). As mentioned above, the SST anomalous dipole in the Atlantic sector, except for its further north location, resembles the SAD mode previously associated with variations in the rainy season in western and southeastern Brazil [52]. Considering positive TPO and positive IOBW, the anomalous low-level wind patterns obtained from the PCC of the TPO and WND850 and PCC of the IOBW and WND850 are similar to Bombardi and Carvalho's [52] results regarding the low-level circulation composites in January, respectively, for the negative and positive SAD modes (their Figure 5c,d). The difference is that the circulation in the TSA in the present analysis features closed anomalous vortexes, which represent intensified and weakened SASH pressure systems (Figure 8a,b).

The abovementioned low-level circulation anomaly patterns are part of the tropical heat induced large-scale circulation anomaly patterns, which can be inferred from the PCC maps for the asymmetric streamfunction (Figure 9). For positive TPO, the map of the PCC of the TPO and PSI200 suggests a Matsuno-Gill-type atmospheric response to the EN-related heating [54,55] and describes anomalous vortex couplets between 35° N and 30° S straddling the equator, which are anticyclonic in the central-eastern Pacific and cyclonic in the Indo-Asian and the South American–Atlantic–African regions (Figure 9a). The PSA pattern is quite evident, and an anomalous anticyclone is settled in the subtropical TSA. The Rossby wave train pattern associated with the equatorial central Pacific's warming follows a circumglobal waveguide path along the Southern Hemisphere midlatitudes and extratropics obtained from barotropic model experiments [56]. This path starts in the central equatorial Pacific, with an anticyclone, turns southward into the Bellingshausen Sea, and flows east-

ward across the Weddell Sea, South Indian Ocean, and east of Australia returns to tropics (Figure 9a; Figure 13 in Hoskins and Ambrizzi [56]). The PCC map of the TPO and PSI850 also shows anomalous vortex couplets straddling the equator, which are zonally and meridionally more extensive, particularly in the Indo-Asian and Pacific sectors. These vortexes present a baroclinic structure in the tropics and a nearly equivalent barotropic structure in the extratropics and subtropics (Figure 9a,b). It is worth noting that the pairs of vortexes straddling the equator in the South American–Atlantic–African region, which are anticyclonic at 850 hPa and cyclonic at 200 hPa are consistent with the anomalous cooling in the equatorial Atlantic (Figures 8a and 9a,b). The anomalous nearly equivalent barotropic anticyclone in the TSA contributes to intensify the SASH pressure system and holds the abovementioned relationships with the rainfall in SESA (Figures 6b, 7a, 8a and 9b).

In relation to the maps of the PCC of the TPO and stream function in upper and lower tropospheric levels, the corresponding maps of the PCC of the IOBW index show smaller magnitudes of the correlations and more horizontal structure at the 850 hPa (Figure 9). For the positive IOBW, the map of the PCC of the IOBW and PSI850 shows pairs of anomalous vortexes straddling the equator in the western Pacific–Indonesian–Australian sector (anticyclones), eastern SA-Atlantic sector (cyclones), central Pacific (anticyclones), and western Indian Ocean (cyclones), with the northern center of the pairs in the two latter regions extended into the subtropics (Figure 9d). Additionally, for the positive IOBW, the map of the PCC of the IOBW and PSI200 suggests a Matsuno-Gill-type atmospheric response to the anomalous heating in the equatorial Atlantic with one anticyclone over eastern tropical SA and its counterpart in western TNA (Figures 8b and 9c; Matsuno [54]; Gill [55]). This anomalous heating source induces a Rossby wave train pattern identified at 200 hPa that starts in tropical SA with an anticyclone, turns southeastward into South Atlantic with a cyclone, reaches the Weddell Sea, then follows approximately the theoretical circumglobal waveguide path along the Southern Hemisphere midlatitudes and extratropics and east of Australia it returns back to tropics (Figure 9a; Figure 13 in Hoskins and Ambrizzi [56]). The vortex shows a baroclinic structure over tropical SA with upper-level anticyclone and low-level cyclone, and a dipole-like equivalent barotropic pattern with an anticyclone in the extratropical South Atlantic and a cyclone in the TSA, which concurs to the circulation anomalies in the South American–Atlantic region (Figures 8b and 9c,d). Additionally, both maps of the PCC of the IOBW and PSI200 and the PCC of the TPO and PSI200 present a Rossby wave train pattern that follows the theoretical path in the southern midlatitudes and extratropics, what indicates modulations by the austral summer southern jet.

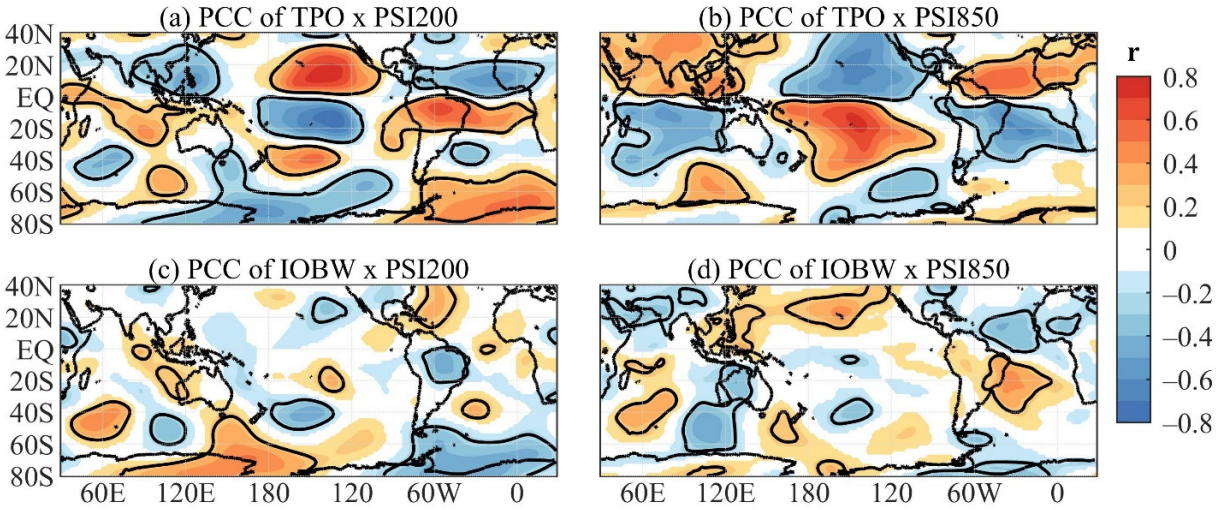

Figure 9. Partial correlations for the asymmetric streamfunction during summer of the (**a**) TPO and PSI200; (**b**) TPO and PSI850; (**c**) IOBW and PSI200; (**d**) IOBW and PSI850. Continuous line encompasses significant correlations at a 95% confidence level using Student's *t*-test.

4. Discussion and Conclusions

The EN in the tropical Pacific and the warm IOBW in the tropical Indian Ocean co-exist and affect the climate in regions distant from their action centers. Previously, Taschetto and Ambrizzi [17] studied the warm IOBW event's effect on autumn rainfall in SA while excluding the EN effect. The focus here is on the relative role of the two events in the summer rainfall in SA during the 1951–2016 period. The PC time series of the first EOF modes of the SST anomalies in the tropical Pacific and the tropical Indian Ocean calculated separately referred to as the TPO and IOBW indices, were used to represent the temporal variations of the ENSO and IOBW modes, respectively. The analyses here are mostly based on the PCC of a given oceanic index (TPO or IOBW) and the variables.

The map of the TCC of the TPO and rainfall describes the combined IOBW and ENSO effects on the South American rainfall and depicts a dipole like pattern between the northwestern–northern SA and SESA (Figure 6a). For the positive TPO, this dipole features a dry–wet pattern. It was previously attributed to the EN-induced atmospheric circulation anomalies with the anomalously eastward-displaced Walker cell justifying the rainfall deficits in equatorial SA [5–7], and an intensified SALLJ, through the associated regional moisture transport, the excessive rainfall in SESA [1,9]. Nevertheless, the IOBW and ENSO modes, both in their warm or cold phases, independently have distinct effects on the South American rainfall (Figure 6b,c).

The EN without the warm IOBW effects induces an anomalous dry–wet dipole between the eastern Amazon–most of NEB and part of SESA (Uruguay, southern Brazil and northeastern Argentina) (Figure 6b). The northern dry node is consistent with the EN-related anomalous sinking motions of the Walker and Hadley cells and strong moisture divergence over northern SA, adjacent oceanic areas, equatorial Atlantic and along eastern SA north of 20° S, and the southern wet node is consistent with moisture convergence over eastern and southern Brazil, Uruguay and the adjacent oceanic areas (Figures 4a, 5a, 6b and 7a). The moisture divergence–convergence pattern is associated with a vigorous anticyclone over TSA and SA east of 60° W whose northwestern–southeastern edge likely intensifies the SALLJ, which transports moisture from the Amazon southeastward into SESA, where convergent moisture flux and excessive rainfall occur (Figures 6b and 7a). This result is consistent with the previous finding regarding the EN effect on the South American rainfall [1,2]. On the other hand, the warm IOBW without the EN effects drives an anomalous wet–dry dipole between NEB and part of southeastern Brazil (Figure 6c). This anomalous rainfall dipole seems to be more closely modulated by the regional atmospheric circulation anomalies with an anticyclone over SA between the equator and 20° S, and a cyclone in the southwestern Atlantic between 20° S and 40° S. These regional circulation anomalies lead the moisture convergence over equatorial Atlantic and along eastern SA between the equator and 20° S and moisture divergence over coastal areas of southeastern Brazil and the adjacent Atlantic (Figures 4b, 5b and 7b).

The abovementioned differential anomalous atmospheric circulation patterns over SA and neighboring areas associated with the isolated effects of the EN and warm IOBW events are part of the large-scale circulation anomalies associated with the differential positions of the tropical heat sources (Figure 3). In the case of the isolated EN effect, the warming in the equatorial Pacific is the only heat source nearly symmetric about the equator in the tropical sector. Consequently, the Matsuno-Gill-type atmospheric response to the EN-related heating induces anomalous vortex couplets between 35° N and 30° S straddling the equator, which in the upper tropospheric levels are anticyclonic in the central-eastern Pacific and cyclonic in the Indo-Asian and the South American–Atlantic–African regions and vice versa in the lower tropospheric levels (Figure 9a,b). The baroclinic vortex, anticyclonic at 850 hPa and cyclonic at 200 hPa over the tropical SA-Atlantic sector, is consistent with the abovementioned low-level anticyclone associated with dryness over eastern Amazon and NEB (Figures 6b, 7a, 8a and 9a,b). In the subtropical TSA, the anomalous barotropic equivalent anticyclone associated with the PSA pattern explains the moisture transport into SESA (Figures 6b, 7a and 9a,b).

Nevertheless, under the isolated influence of the warm IOBW, two tropical heat sources coexist one in the tropical Indian Ocean, which is not symmetric about the equator, and the other symmetric about the equator in the Atlantic (Figure 3b). It is interesting to note that the atmospheric response to the Indian Ocean heat source is much weaker than for the Atlantic heat source. Indeed, the anomalous ascending motions along the vertical-equatorial plane are relatively weak over the Indian Ocean longitudes and strong over the Atlantic longitudes (Figure 4b). Consequently, the Matsuno-Gill-type atmospheric response to the equatorial Atlantic heating induces pairs of anomalous vortexes straddling the equator in the South American–Atlantic sector, which are cyclonic over tropical Atlantic and eastern SA in lower tropospheric levels and, anticyclonic over tropical SA and western TNA in upper tropospheric level. The 850 hPa cyclone over tropical SA is consistent with the anomalous wetness over NEB (Figures 6c, 7b, 8b and 9c,d). Additionally, an anomalous barotropic equivalent cyclone is settled in the subtropical TSA in association with the Rossby wave train that emanates from the equatorial Atlantic heat source (Figures 8b and 9c,d). This cyclone is consistent with the anomalous dryness over southeastern Brazil (Figure 6c).

The results here indicate that the relationship between the tropical Indian Ocean warming and rainfall variability in SA during austral summer does not occur through a Rossby wave train pattern connecting that oceanic region and SA, but indirectly by means of the SST variations in the Atlantic, which are, in turn modulated by the regional atmospheric circulation alterations associated with the Indian Ocean warming. One reason seems that the main warming in the Indian Ocean does not induce a strong atmospheric response. In fact, a weak low-level cyclone south of the equator in the western Indian Ocean forms a pair with the cyclone over the North Arabian Sea, Pakistan, and northwestern India (Figure 9d). Since the circulation associated with the IOBW shows a barotropic structure in southwest Asia (Figure 9c,d), our results are consistent with previous findings on the Rossby wave generated by the tropical Indian Ocean warming with an upper-level trough over southwest Asia [57,58]. Our results are also consistent with Liao and Wang [59], who documented a connection between the warming in the tropical Indian Ocean and a warming in the equatorial Atlantic during the austral summer. Another possibility is that the southern jet during summer plays a crucial role in capturing the Rossby wave train patterns along the theoretical path [56] in the South Indian Ocean, such that after Australia the wave train turns back to the tropics (Figure 9c,d).

Since the correlation analysis implies linear relations, composite analysis was performed for precipitation to examine some nonlinear relations between the TPO and IOBW indices and the precipitation over SA. Firstly, the effect of one index in the other was removed using linear regression (least squares method), and the residual TPO and residual IOBW indices were constructed. Additionally, the residual precipitation anomalies without the TPO or IOBW effects were obtained. Then, composites of the residual precipitation anomalies without IOBW effects for residual TPO > 0.5, TPO < −0.5 (Figure 10a,b), of residual precipitation anomalies without the TPO effects for residual IOBW > 0.5 and IOBW < −0.5 (Figure 10c,d) were obtained. Figure 10a,b shows, in general, antisymmetric rainfall responses to TPO > 0.5 and TPO < −0.5, except in eastern SA east of 50° W and between approximately 5° S and 25° S, with a larger meridional extension of the significant negative precipitation anomalies for the TPO > 0.5 composite than of the positive ones for the TPO < −0.5 composite. On the other hand, better organized significant negative precipitation anomalies are found over NEB and central-eastern SA for the IOBW < −0.5 composite (Figure 10d) than the positive ones in this same area for the IOBW > 0.5 composite (Figure 10c). The asymmetries between negative and positive precipitation anomalies for the TPO > 0.5 and TPO < −0.5 composites and for the IOBW > 0.5 and IOBW < −0.5 composites indicate the nonlinear rainfall responses to these two oceanic modes. These figures also illustrate similar magnitudes of the precipitation anomalies for the TPO and IOBW composites. Therefore, these analyses validate our conclusions based on the correlation analyses.

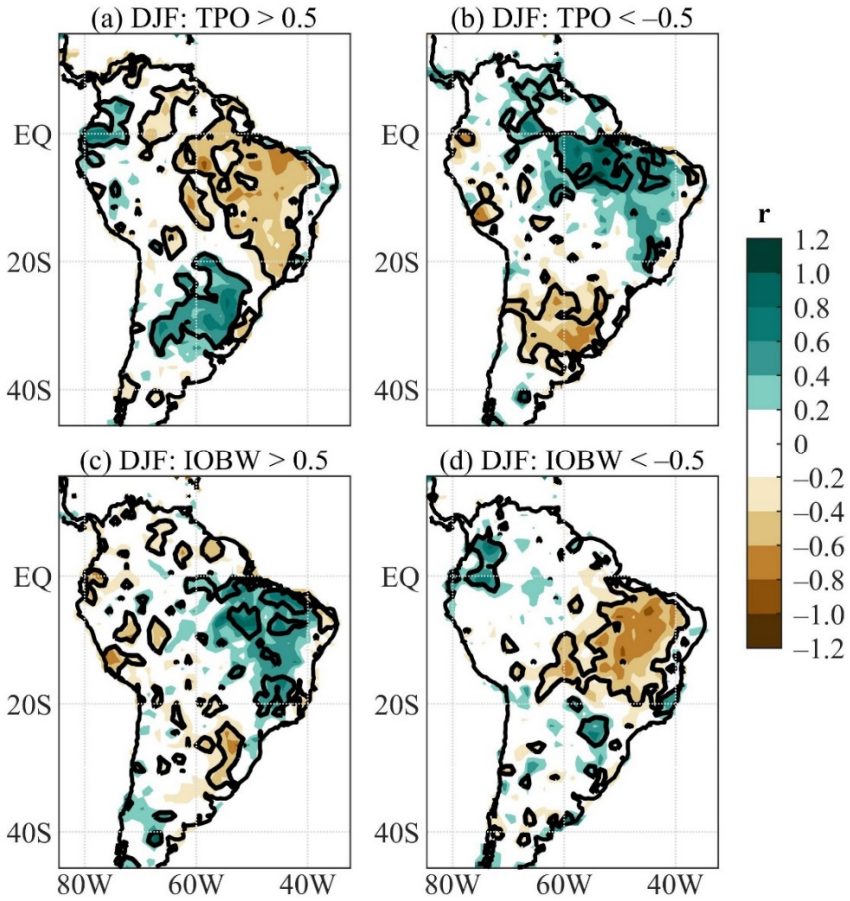

Figure 10. Composite analyses of residual precipitation anomalies for (**a**) TPO > 0.5; (**b**) TPO < −0.5; (**c**) IOBW > 0.5; (**d**) IOBW < −0.5. Continuous line encompasses the significant values at a 95% confidence level using Student's *t*-test.

The correlation analyses above refer to the EN and warm IOBW events. However, for the LN and cold IOBW events, the opposite patterns of the rainfall and atmospheric circulation anomalies can be inferred. The approach adopted here by isolating the EN and warm IOBW event effects on the rainfall over SA provided useful information for monitoring tasks during ENSO neutral years. The independent responses to the TPO and IOBW modes show spatial variability of the rainfall, with the modes reinforcing each other their effects in regions north of the equator and counteracting each other in some regions like southeastern Brazil and NEB, but the TPO has a dominant effect in SESA (Figures 6 and 7). The contrasting effect over eastern Brazil areas (southeastern and northeastern) could be the thermodynamic response to the contrasting SST anomalies in equatorial and TSA induced independently by the Indian and Pacific Oceans (Figure 8). Since large portions of SA experience the rainy season during austral summer, the results here strongly suggest that monitoring the tropical Indian Ocean during the ENSO developing phase might be very important for practical purposes.

Author Contributions: Conceptualization—M.T.K., W.L.C. and R.V.A. Methodology—M.T.K., R.V.A., W.L.C. Software was managed by M.T.K., W.L.C. and R.A.F.S. Validation—M.T.K., R.V.A. and W.L.C., Formal analysis—M.T.K., R.V.A., W.L.C. and R.A.F.S. Investigation—M.T.K., R.V.A. and W.L.C. Data curation—M.T.K. and W.L.C. Original draft preparation—M.T.K., R.V.A. and W.L.C. Reviewing and editing—M.T.K., R.V.A., W.L.C. and R.A.F.S. Visualization—M.T.K. and W.L.C. Supervision—M.T.K. All authors have read and agreed to the published version of the manuscript.

Funding: The Conselho Nacional de Desenvolvimento Científico e Tecnológico (CNPq) of Brazil partially supported the first and second authors under grants 302322/2017-5, and 305611/2019-4, respectively. The third author was partially supported by Project 65146 of the Convocatoria 818 of

2018–Colciencias, IC-21106 from the Universidad del Valle (Cali-Colombia). "Support for the National Centers for Environmental Prediction/National Center for Atmospheric Research (NCEP/NCAR) Reanalysis-I Project dataset was provided by the National Oceanic and Atmospheric Administration/Earth System Research Laboratories/Physical Sciences Laboratory (NOAA/ESRL/PSL)". "Support for the extended reconstructed SST version V5 dataset and for the precipitation GPCC dataset was provided by NOAA/ESRL/PSL". The authors thank the four anonymous reviewers for their helpful comments.

Institutional Review Board Statement: Not applicable.

Informed Consent Statement: Not applicable.

Data Availability Statement: Not appliable.

Conflicts of Interest: The authors declare no conflict of interest. The founding sponsors had no role in the design, analysis, and interpretation of data, in the writing manuscript, or in the decision to publish the results.

References

1. Zhou, J.; Lau, K.M. Principal modes of interannual and decadal variability of summer rainfall over South America. *Int. J. Climatol.* **2001**, *21*, 1623–1644. [CrossRef]
2. Grimm, A.M.; Ambrizzi, T. Teleconnections into South America from the Tropics and Extratropics on Interannual and Intraseasonal Timescales. In *Past Climate Variability in South America and Surrounding Regions. Developments in Paleoenvironmental Research*; Vimeux, F., Sylvestre, F.K.M., Eds.; Springer: Dordrecht, The Netherlands, 2009; pp. 159–191. ISBN 9789048126729.
3. Mo, K.C.; Higgins, R.W. The Pacific-South American modes and tropical convection during the Southern Hemisphere winter. *Mon. Weather Rev.* **1998**, *126*, 1581–1596. [CrossRef]
4. Paegle, J.N.; Mo, K.C. Linkages between summer rainfall variability over South America and sea surface temperature anomalies. *J. Clim.* **2002**, *15*, 1389–1407. [CrossRef]
5. Ropelewski, C.F.; Halpert, M.S. Global and Regional scale precipitation patterns associated with the El Niño-Southern Oscillation. *Mon. Weather Rev.* **1987**, *115*, 1606–1626. [CrossRef]
6. Kousky, V.E.; Kagano, M.T.; Cavalcanti, I.F.A. A review of the Southern Oscillation: Oceanic-atmospheric circulation changes and related rainfall anomalies. *Tellus A* **1984**, *36A*, 490–504. [CrossRef]
7. Kayano, M.T.; Rao, V.B.; Moura, A.D. Tropical circulations and the associated rainfall anomalies during two contrasting years. *J. Climatol.* **1988**, *8*, 477–488. [CrossRef]
8. Grimm, A.M.; Ferraz, S.E.T.; Gomes, J. Precipitation Anomalies in Southern Brazil Associated with El Niño and La Niña Events. *J. Clim.* **1998**, *11*, 2863–2880. [CrossRef]
9. Grimm, A.M. The El Niño Impact on the Summer Monsoon in Brazil: Regional Processes versus Remote Influences. *J. Clim.* **2003**, *16*, 263–280. [CrossRef]
10. Grimm, A.M.; Pal, J.S.; Giorgi, F. Connection between spring conditions and peak summer monsoon rainfall in South America: Role of soil moisture, surface temperature, and topography in eastern Brazil. *J. Clim.* **2007**, *20*, 5929–5945. [CrossRef]
11. Kousky, V.E.; Ropelewski, C.F. Extremes in the Southern Oscillation and their Relationship to Precipitation Anomalies with Emphasis on the South American Region. *Rev. Bras. Meteorol.* **1989**, *4*, 351–363.
12. Cai, W.; McPhaden, M.J.; Grimm, A.M.; Rodrigues, R.R.; Taschetto, A.S.; Garreaud, R.D.; Dewitte, B.; Poveda, G.; Ham, Y.-G.; Santoso, A.; et al. Climate impacts of the El Niño–Southern Oscillation on South America. *Nat. Rev. Earth Environ.* **2020**, *1*, 215–231. [CrossRef]
13. Wang, C. Three-ocean interactions and climate variability: A review and perspective. *Clim. Dyn.* **2019**, *53*, 5119–5136. [CrossRef]
14. Chambers, D.P.; Tapley, B.D.; Stewart, R.H. Anomalous warming in the Indian Ocean coincident with El Niño. *J. Geophys. Res. Ocean* **1999**, *104*, 3035–3047. [CrossRef]
15. Annamalai, H.; Xie, S.P.; McCreary, J.P.; Murtugudde, R. Impact of Indian Ocean Sea surface temperature on developing El Niño. *J. Clim.* **2005**, *18*, 302–320. [CrossRef]
16. Xie, S.P.; Hu, K.; Hafner, J.; Tokinaga, H.; Du, Y.; Huang, G.; Sampe, T. Indian Ocean capacitor effect on Indo-Western Pacific climate during the summer following El Niño. *J. Clim.* **2009**, *22*, 730–747. [CrossRef]
17. Taschetto, A.S.; Ambrizzi, T. Can Indian Ocean SST anomalies influence South American rainfall? *Clim. Dyn.* **2012**, *38*, 1615–1628. [CrossRef]
18. Klein, S.A.; Soden, B.J.; Lau, N.-C. Remote Sea Surface Temperature Variations during ENSO: Evidence for a Tropical Atmospheric Bridge. *J. Clim.* **1999**, *12*, 917–932. [CrossRef]
19. Deser, C.; Alexander, M.A.; Xie, S.P.; Phillips, A.S. Sea surface temperature variability: Patterns and mechanisms. *Ann. Rev. Mar. Sci.* **2010**, *2*, 115–143. [CrossRef] [PubMed]
20. Lau, N.C.; Nath, M.J. Atmosphere-ocean variations in the Indo-Pacific sector during ENSO episodes. *J. Clim.* **2003**, *16*, 3–20. [CrossRef]

21. Saji, N.H.; Goswani, B.N.; Vinayachandran, P.N.; Yamagat, T. A dipole mode in the tropical Indian Ocean. *Nature* **1999**, *401*, 360–363. [CrossRef] [PubMed]
22. Webster, P.J.; Moore, A.M.; Loschnigg, J.P.; Leben, R.R. Coupled ocean-atmosphere dynamics in the Indian Ocean during 1997–1998. *Nature* **1999**, *401*, 356–360. [CrossRef]
23. Ashok, K.; Guan, Z.; Yamagata, T. Impact of the Indian Ocean dipole on the relationship between the Indian monsoon rainfall and ENSO. *Geophys. Res. Lett.* **2001**, *28*, 4499–4502. [CrossRef]
24. Clark, C.O.; Webster, P.J.; Cole, J.E. Interdecadal variability of the relationship between the Indian Ocean zonal mode and East African coastal rainfall anomalies. *J. Clim.* **2003**, *16*, 548–554. [CrossRef]
25. Cai, W.; Cowan, T.; Raupach, M. Positive Indian Ocean Dipole events precondition southeast Australia bushfires. *Geophys. Res. Lett.* **2009**, *36*, 1–6. [CrossRef]
26. Saji, N.H.; Ambrizzi, T.; Ferraz, S.E.T. Indian Ocean Dipole mode events and austral surface air temperature anomalies. *Dyn. Atmos. Ocean* **2005**, *39*, 87–101. [CrossRef]
27. Chan, S.C.; Behera, S.K.; Yamagata, T. Indian Ocean Dipole influence on South American rainfall. *Geophys. Res. Lett.* **2008**, *35*, 10–14. [CrossRef]
28. Drumond, A.R.d.M.; Ambrizzi, T. The role of the South Indian and Pacific oceans in South American monsoon variability. *Theor. Appl. Climatol.* **2008**, *94*, 125–137. [CrossRef]
29. González, M.H.; Skansi, M.M.; Losano, F. A statistical study of seasonal winter rainfall prediction in the Comahue region (Argentina). *Atmosfera* **2010**, *23*, 277–294.
30. González, M.H.; Vera, C.S. On the interannual wintertime rainfall variability in the Southern Andes. *Int. J. Climatol.* **2010**, *30*, 643–657. [CrossRef]
31. Berman, A.L.; Silvestri, G.; Compagnucci, R.; Velasco Herrera, V. Oceanic influence on southernmost South American precipitation. *Atmosfera* **2012**, *25*, 217–233.
32. Han, W.; Vialard, J.; McPhaden, M.J.; Lee, T.; Masumoto, Y.; Feng, M.; De Ruijter, W.P.M. Indian ocean decadal variability: A review. *Bull. Am. Meteorol. Soc.* **2014**, *95*, 1679–1703. [CrossRef]
33. Cai, W.; Wu, L.; Lengaigne, M.; Li, T.; McGregor, S.; Kug, J.S.; Yu, J.Y.; Stuecker, M.F.; Santoso, A.; Li, X.; et al. Pantropical climate interactions. *Science* **2019**, *363*, eaav4236. [CrossRef]
34. Alory, G.; Wijffels, S.; Meyers, G. Observed temperature trends in the Indian Ocean over 1960–1999 and associated mechanisms. *Geophys. Res. Lett.* **2007**, *34*, 2–7. [CrossRef]
35. Du, Y.; Xie, S.P. Role of atmospheric adjustments in the tropical Indian Ocean warming during the 20th century in climate models. *Geophys. Res. Lett.* **2008**, *35*, 2–6. [CrossRef]
36. Dong, L.; Zhou, T.; Wu, B. Indian Ocean warming during 1958–2004 simulated by a climate system model and its mechanism. *Clim. Dyn.* **2014**, *42*, 203–217. [CrossRef]
37. Roxy, M.K.; Ritika, K.; Terray, P.; Masson, S. The curious case of Indian Ocean warming. *J. Clim.* **2014**, *27*, 8501–8509. [CrossRef]
38. Rao, V.B.; Hada, K. Characteristics of rainfall over Brazil: Annual variations and connections with the Southern Oscillation. *Theor. Appl. Climatol.* **1990**, *42*, 81–91. [CrossRef]
39. Rasmusson, E.M.; Arkin, P.A. Interannual climate variability associated with the El Niño/ Southern Oscillation. *Elsevier Oceanogr. Ser.* **1985**, *40*, 697–725.
40. Huang, B.; Thorne, P.W.; Banzon, V.F.; Boyer, T.; Chepurin, G.; Lawrimore, J.H.; Menne, M.J.; Smith, T.M.; Vose, R.S.; Zhang, H.M. Extended reconstructed Sea surface temperature, Version 5 (ERSSTv5): Upgrades, validations, and intercomparisons. *J. Clim.* **2017**, *30*, 8179–8205. [CrossRef]
41. National Oceanic and Atmospheric Administration; Extended Reconstructed Sea Surface Temperature (NOAA/ERSST) SST Data. Available online: https://www.esrl.noaa.gov/psd/data/gridded/ (accessed on 1 March 2018).
42. Schneider, U.; Becker, A.; Finger, P.; Meyer-Christoffer, A.; Ziese, M.; Rudolf, B. GPCC's new land surface precipitation climatology based on quality-controlled in situ data and its role in quantifying the global water cycle. *Theor. Appl. Climatol.* **2014**, *115*, 15–40. [CrossRef]
43. Global Precipitation Climatology Centre (GPCC) Monthly Gridded Precipitation Data. Available online: https://www.esrl.noaa.gov/psd/data/gridded/data.gpcc.html (accessed on 3 May 2019).
44. Kalnay, E.; Kanamitsu, M.; Kistler, R.; Collins, W.; Deaven, D.; Gandin, L.; Iredell, M.; Saha, S.; White, G.; Woollen, J.; et al. The NCEP/ NCAR reanalysis project. *Bull. Amer. Meteor. Soc.* **1996**, *77*, 437–471. [CrossRef]
45. National Center for Environmental Prediction; National Center for Atmospheric Research (NCEP/NCAR) Reanalysis-I Project Dataset. Available online: https://psl.noaa.gov/data/gridded/ (accessed on 3 September 2020).
46. Peixoto, J.P.; Oort, A.H. *Physics of Climate*; MIT Press: San Diego, CA, USA, 1992; ISBN 7287064.
47. Torrence, C.; Compo, G.P. A Practical Guide to Wavelet Analysis Christopher. *Bull. Am. Meteorol. Soc.* **1998**, *97*, 61–78. [CrossRef]
48. North, G.L.; Bell, T.L.; Chalan, R.F. Sampling Errors in the Estimtion of Empirical Othogonal Functions. *Mon. Weather Rev.* **1982**, *110*, 699–706. [CrossRef]
49. Panofsky, H.G.; Brier, G.W. *Some Applications of Statistics to Meteorology*; Earth and Mineral Sciences Continuing Education, College of Earth and Mineral Sciences, Ed.; Pennsylvania State University: Pennsylvania, PA, USA, 1968.
50. Rasmusson, E.M.; Wallace, J.M. Meteorological Aspects of the El Niño/Southern Oscillation. *Science* **1983**, *222*, 1195–1202. [CrossRef]

51. An, S.I.; Jin, F.F. Nonlinearity and asymmetry of ENSO. *J. Clim.* **2004**, *17*, 2399–2412. [CrossRef]
52. Bombardi, R.J.; Carvalho, L.M.V. The South Atlantic dipole and variations in the characteristics of the South American Monsoon in the WCRP-CMIP3 multi-model simulations. *Clim. Dyn.* **2011**, *36*, 2091–2102. [CrossRef]
53. Kayano, M.T.; Andreoli, R.V.; Ferreira de Souza, R.A. Relations between ENSO and the South Atlantic SST modes and their effects on the South American rainfall. *Int. J. Climatol.* **2013**, *33*, 2008–2023. [CrossRef]
54. Matsuno, T. Quasi-Geostrophic Motions in the Equatorial Area. *J. Meteorol. Soc. Japan. Ser. II* **1966**, *44*, 25–43. [CrossRef]
55. Gill, A.E. Some simple solutions for heat-induced tropical circulation. *Q. J. R. Meteorol. Soc.* **1980**, *106*, 447–462. [CrossRef]
56. Hoskins, B.J.; Ambrizzi, T. Rossby wave propagation on a realistic longitudinally varying flow. *J. Atmos. Sci.* **1993**, *50*, 1661–1671. [CrossRef]
57. Abid, M.A.; Ashfaq, M.; Kucharski, F.; Evans, K.J.; Almazroui, M. Tropical Indian Ocean mediates ENSO influence over central Southwest Asia during the Wet Season. *Geophys Res Lett.* **2020**, *47*, e2020GL089308. [CrossRef]
58. Abid, M.A.; Kucharski, F.; Molteni, F.; Kang, I.S.; Tompkins, A.M.; Almazroui, M. Separating the Indian and Pacific Ocean impacts on the Euro-Atlantic response to ENSO and its transition from early to late winter. *J. Clim.* **2021**, *34*, 1531–1548. [CrossRef]
59. Liao, H.; Wang, C. Sea Surface temperature Anomalies in the Western Indian Ocean as a Trigger for Atlantic Niño Events. *Geophys. Res Lett.* **2021**, *48*, e2021GL092489. [CrossRef]